Traces of surfactants can severely limit the drag reduction of superhydrophobic surfaces

François J. Peaudecerf[a], Julien R. Landel[b], Raymond E. Goldstein[a], and Paolo Luzzatto-Fegiz[c,1]

[a]Department of Applied Mathematics and Theoretical Physics, Centre for Mathematical Sciences, University of Cambridge, Cambridge CB3 0WA, United Kingdom; [b]School of Mathematics, University of Manchester, Manchester M13 9PL, United Kingdom; and [c]Department of Mechanical Engineering, University of California, Santa Barbara, CA 93106

Edited by William R. Schowalter, Princeton University, Princeton, NJ, and approved May 23, 2017 (received for review February 13, 2017)

Superhydrophobic surfaces (SHSs) have the potential to achieve large drag reduction for internal and external flow applications. However, experiments have shown inconsistent results, with many studies reporting significantly reduced performance. Recently, it has been proposed that surfactants, ubiquitous in flow applications, could be responsible by creating adverse Marangoni stresses. However, testing this hypothesis is challenging. Careful experiments with purified water already show large interfacial stresses and, paradoxically, adding surfactants yields barely measurable drag increases. To test the surfactant hypothesis while controlling surfactant concentrations with precision higher than can be achieved experimentally, we perform simulations inclusive of surfactant kinetics. These reveal that surfactant-induced stresses are significant at extremely low concentrations, potentially yielding a no-slip boundary condition on the air–water interface (the "plastron") for surfactant concentrations below typical environmental values. These stresses decrease as the stream-wise distance between plastron stagnation points increases. We perform microchannel experiments with SHSs consisting of stream-wise parallel gratings, which confirm this numerical prediction, while showing near-plastron velocities significantly slower than standard surfactant-free predictions. In addition, we introduce an unsteady test of surfactant effects. When we rapidly remove the driving pressure following a loading phase, a backflow develops at the plastron, which can only be explained by surfactant gradients formed in the loading phase. This demonstrates the significance of surfactants in deteriorating drag reduction and thus the importance of including surfactant stresses in SHS models. Our time-dependent protocol can assess the impact of surfactants in SHS testing and guide future mitigating designs.

superhydrophobic surface | drag reduction | surfactant | Marangoni stress | plastron

Superhydrophobic surfaces (SHSs) combine hydrophobic surface chemistry and micro- or nanoscale patterning to retain a network of air pockets when exposed to a liquid (e.g., reviews in refs. 1–3). Because a large portion of the interface between the solid wall and the liquid is replaced by an air–liquid interface, which can be considered almost as a shear-free surface (known as a "plastron"), SHSs could be used to obtain significant drag reduction in fluid flow applications (4, 5). Microchannel tests have recorded drag reductions of over 20% (e.g., refs. 6–11) and rheometer tests reported slip lengths of up to 185 μm (12). Turbulent flow experiments have reduced drag by up to 75% (13–16). However, a wide range of experiments have provided inconsistent results, with several studies reporting little or no drag reduction (16–25).

A key step toward solving this puzzle has come with the realization that surfactants could induce Marangoni stresses that impair drag reduction. This was first hypothesized to account for experiments that revealed little measurable slip (23, 24), in contradiction with available theoretical predictions based on the absence of surfactants (26–34). Following this hypothesis, surfactants naturally present in water would adsorb onto the air–water interface, as sketched in Fig. 1*A*, and they would be advected by the flow and therefore accumulate at downstream stagnation points, where the interface terminates in a three-phase contact line. The resulting surfactant gradient would then yield a Marangoni stress resisting the fluid motion, thereby decreasing slip and increasing drag (Fig. 1*B*). Traditional models of SHSs are surfactant-free and therefore do not account for this additional drag. This is especially concerning for marine applications, because it is well documented that seawater contains significant amounts of surfactants (35). Rivers, estuaries, and fog also show significant levels of both synthetic and natural surfactants (36, 37).

Recent experiments have shown that whereas a nominally clean flow already displayed slip that was several times below predictions of surfactant-free theories, adding large amounts of surfactant had a barely measurable effect (38). This counterintuitive result appears to undermine the surfactant hypothesis, which would come with the expectation of a strong sensitivity to surfactant concentration. Proving or disproving the surfactant hypothesis, while resolving the above paradox, is essential to design SHSs that can achieve large, reliable drag reduction.

Simulations with Detailed Kinetics

To investigate the flow at extremely low surfactant concentrations, which are essentially impossible to accurately prescribe in experiments, we developed a computational tool for simulating surfactant-laden flows over an SHS whose plane geometry is shown in Fig. 2*A* (full transport model in *SI Model*, *SI Materials and Methods*, and Tables S1 and S2). Neglecting air viscosity, we

Significance

Whereas superhydrophobic surfaces (SHSs) have long promised large drag reductions, experiments have provided inconsistent results, with many textures yielding little or no benefit. Given the vast potential impact of SHSs on energy utilization, finding an explanation and mitigating strategies is crucially important. A recent hypothesis suggests surfactant-induced Marangoni stresses may be to blame. However, paradoxically, adding surfactants has a barely measurable effect, casting doubt on this hypothesis. By performing surfactant-laden simulations and unsteady experiments we demonstrate the impact of surfactants and how extremely low concentrations, unavoidable in practice, can increase drag up to complete immobilization of the air–liquid interface. Our approach can be used to test other SHS textures for sensitivity to surfactant-induced stresses.

Author contributions: F.J.P., J.R.L., R.E.G., and P.L.-F. designed research, performed research, analyzed data, and wrote the paper.

The authors declare no conflict of interest.

This article is a PNAS Direct Submission.

[1] To whom correspondence should be addressed. Email: fegiz@engineering.ucsb.edu.

This article contains supporting information online at www.pnas.org/lookup/suppl/doi:10.1073/pnas.1702469114/-/DCSupplemental.

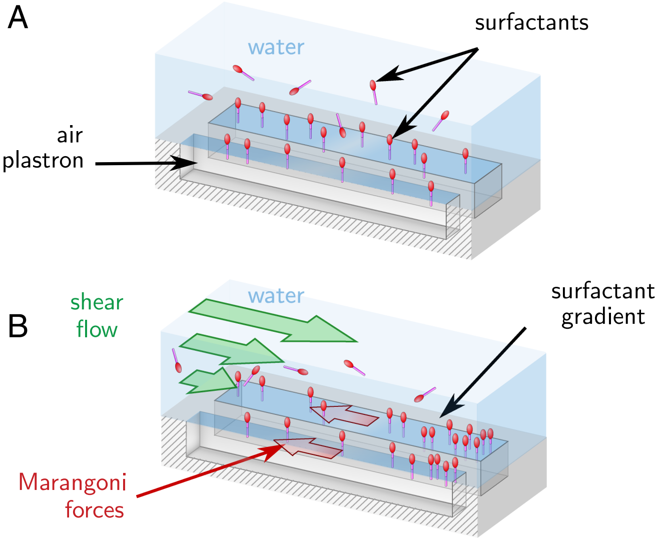

Fig. 1. Presence of surfactants as contaminants can generate Marangoni forces on an SHS. (*A*) Surfactants present in water adsorb at the air–water interface of SHSs. (*B*) In the presence of an external flow, surfactants distribute in gradients between stagnation points. From these gradients Marangoni forces result, resisting the flow and immobilizing the interface.

consider a 2D air–water interface of length g on which surfactants from the bulk can adsorb/desorb and generate Marangoni forces. This interface (in pink in Fig. 2 *A–C*) is on the top of a chamber of depth H and bounded by no-slip ridges of length $\ell/2$ each. The top of the chamber, of length $g+l$, represents a basis element of an SHS. The flow in the chamber is forced by a Poiseuille profile $u(z)$ at $x=0$. In Fig. 2 *B–D*, we show simulation results from very low surfactant concentration to high concentration in the bulk, using the properties of the well-characterized surfactant sodium dodecyl sulfate (SDS) (39). For very low concentration, $c_0 = 10^{-6}$ mM, the corresponding flow velocity is shown in Fig. 2*B*, with gap length $g = 100\ \mu\text{m}$, wall length $\ell = 50\ \mu\text{m}$, channel height $H = 100\ \mu\text{m}$, and forced Poiseuille flow at $x = 0$ of peak speed $50\ \mu\text{m}\cdot\text{s}^{-1}$. The flow field is essentially identical to that for pure water: i.e., $c_0 = 0$. Fig. 2*D* shows the effect of increasing bulk surfactant concentration on the characteristic drag $\langle\tau\rangle$, which has been spatially averaged over one SHS element of length $g+\ell$. The data, from steady-state simulations with other parameters fixed, are normalized by the corresponding wall shear stress τ_{P} of the forcing Poiseuille flow. The case $c_0 = 10^{-6}$ mM, highlighted by the left arrow in Fig. 2*D*, is indeed close to the ideal free-slip drag. The curve in Fig. 2*D* reveals an increase of drag with bulk surfactant concentration, up to the no-slip value, which is reached asymptotically around $c_0 = 10^{-2}$ mM (right arrow in Fig. 2*D*). The corresponding flow velocity is shown in Fig. 2*C*. A large Marangoni stress appears and the slip velocity is reduced by more than one order of magnitude, practically reaching a no-slip boundary condition at the plastron.

For a bulk concentration of just 10^{-2} mM (that is, 10^{-2} mol$\cdot$m^{-3}, corresponding to less than 10 g of surfactants per cubic meter of water), the drag flattens to the no-slip asymptote, after which adding more surfactants has little effect. These results explain why adding surfactants in experiments has a barely measurable effect in most cases, because the transition to a regime where Marangoni stresses dominate occurs at extremely small concentrations. Such small concentrations are very difficult to achieve in laboratory experiments, where controlling surfactant contamination [e.g., from SHS manufacturing and materials, water handling, microscopic-particle image velocimetry (μ-PIV) beads, or any surface or fluid, including air, in contact with the water flowing through the microchannel] is exceedingly difficult. Needless to say, such levels of cleanliness are not found in most flow applications. Surfactants at such low concentrations are essentially impossible to detect using a classical tensiometer apparatus, because the corresponding surface tension decrease, in a static fluid, is negligible (39).

The results presented in Fig. 2*D* are generic to other types of surfactants, as shown in Fig. S1. We also note that the properties of the SDS surfactant used in our study do not induce the strongest Marangoni stresses. In fact, its effect is rather mild compared with the surfactants reported in ref. 40. In normal flow applications, we should therefore assume that stronger surfactants than SDS are likely to be present, thus deteriorating even more the performance of the SHS.

The inevitability of surfactants suggests that the main strategy to minimize Marangoni stresses is to optimize the SHS geometry. To test this hypothesis, we simulate flow over 2D basis elements of SHSs with varying interface length g. By increasing the distance g between the upstream and downstream stagnation points, we reduce the average surfactant gradient over the plastron. Fig. 2*E* shows drag vs. interface length for $c_0 = 10^{-2}$ mM (plotted with red squares). The simulations show that the drag over a contaminated surface is very sensitive to this change of geometry. The drag is also significantly larger than the idealized results for a perfectly clean flow (plotted with red diamonds in Fig. 2*E*) over a large range: $0.01 \leq g \leq 10$ mm.

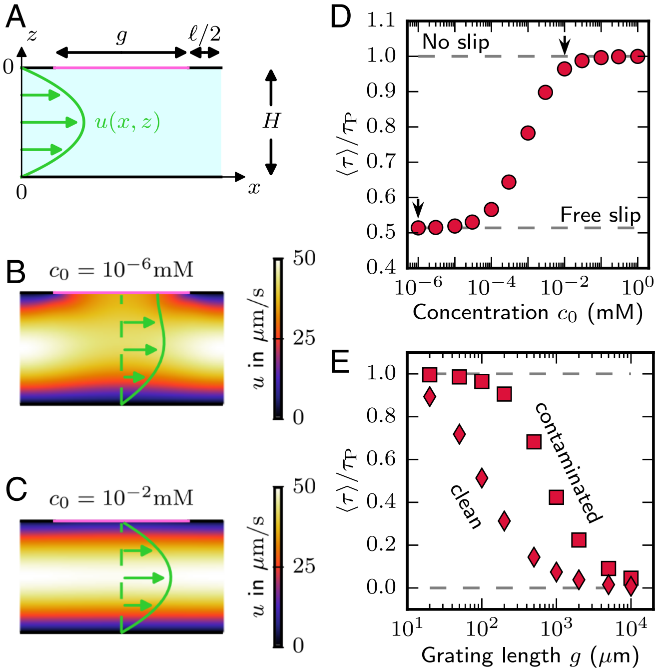

Fig. 2. Numerical simulations of surfactant-laden flows over a 2D SHS. (*A*) Geometry of the simulations for a periodic chamber (i.e., one SHS basis element) of thickness $H = 100\ \mu\text{m}$ with gratings of length $g = 100\ \mu\text{m}$ on the wall at $z = 0$, separated with ridges of length $\ell = 50\ \mu\text{m}$, and with forcing Poiseuille flow at $x = 0$. (*B*) Stream-wise velocity u for bulk surfactant concentration $c_0 = 10^{-6}$ mM, exhibiting slip on the plastron. (*C*) At $c_0 = 10^{-2}$ mM no slip is reached on the plastron. (*D*) Average normalized drag vs. surfactant concentration. An asymptote is reached at concentrations below those found in the environment. (*E*) Drag vs. grating length, for perfectly clean water (red diamonds) and flow with concentration $c_0 = 10^{-2}$ mM (red squares), showing that drag reduction in surfactant-laden flows is very sensitive to grating length. All simulations are performed with a peak velocity of the forcing Poiseuille flow of $50\ \mu\text{m}\cdot\text{s}^{-1}$ and fixed ridge length $\ell = 50\ \mu\text{m}$.

Experiments Show Reduced Slip

To verify the impact of surfactant on plastron slip and the effect of lane length on drag reduction, we performed experiments using μ-PIV on a confocal microscope. We measured the velocity field of gravity-driven microchannel flows in planes parallel to an SHS (Fig. 3 *A*–*C*, *SI Experimental Protocols*, and Tables S3 and S4). Similar to earlier work (10, 13, 24), our SHSs were made of hydrophobic polydimethylsiloxane (PDMS), using photolithography techniques. The SHSs consisted of stream-wise parallel rectangular lanes or gratings, as shown in Fig. 3*B*. The lane width $w = 40$ µm and ridge width $r = 20$ µm were kept fixed in the experiments. The microchannel height varied slightly, $100 \leq H \leq 130$ µm. We sealed the PDMS chamber using a glass coverslip held in place through Van der Waals adhesion, without surface treatment, to avoid surfactant contamination and to preserve PDMS hydrophobicity. The glass coverslip and chamber were maintained at a fixed temperature within 0.1 °C accuracy through cooling elements. This minimized any potential thermal Marangoni effect (as discussed in *SI Experimental Protocols*) and prevented significant condensation inside the gratings, thus ensuring stability of the plastron over several hours. We used purified water in the experiments and cleaned all possible surfaces in contact with water and microbeads, following a strict cleaning protocol (*SI Experimental Protocols*). The microchannel was connected to inlet and outlet reservoirs whose heights were adjusted separately to enable control of both the background pressure gradient and hydrostatic pressure in the microchannel. The plastron was maintained flat through adjustment of the hydrostatic pressure. The interface position was located with an accuracy of 2 µm.

The symbols in Fig. 3*D* show experimental velocity profiles at several horizontal slices in the case of short lanes, $g = 2$ mm (SDs in the velocity are indicated with error bars). For comparison, Fig. 3*D* also shows surfactant-free 3D numerical predictions (plotted with solid lines) for the same geometry (*SI Materials and Methods* and Table S5). Similar to theoretical calculations assuming free slip at the plastron, the surfactant-free numerical simulations predict a very large slip, $\max(u/U) \approx 0.8$ at $z_i/H = 1.6\%$ from the plastron (with U the mean flow speed), whereas experimental data at $z/H \leq 2\%$ show no statistically significant slip. A linear extrapolation using the three data values closest to the interface gives a negligible interfacial slip velocity $u_I/U \approx 0.01 \pm 0.02$. In the case of long lanes (Fig. 3*E*), $g = 30$ mm, experimental data reveal some slip, which is still significantly slower than numerical and theoretical results (26), by ≈85%. A linear extrapolation using the three data values closest to the interface gives $u_I/U \approx 0.14 \pm 0.04$. These results agree with our surfactant-laden simulations reported earlier in Fig. 2*E*: For a given background flow and surfactant concentration, increasing the lane length increases the slip velocity, bringing it closer to predictions from surfactant-free models. This consistency strongly suggests that the reduced slip observed on our experimental SHSs with respect to theoretical predictions comes indeed from traces of unidentified surfactants.

These findings are also consistent with simple scaling analysis. Assuming low interfacial surfactant concentration $\Gamma \ll \Gamma_m$ (with Γ_m the maximum packing concentration) and laminar flow, a force balance at the interface imposes $(1 - u_I/U)/H \sim Ma\langle\Gamma\rangle/(\Gamma_m g)$, with $Ma = 2RT\Gamma_m/(\mu U)$ the Marangoni number, R the gas constant, T the temperature, μ the dynamic viscosity, and $\langle\Gamma\rangle$ the mean concentration over the gap (see *SI Analysis and Discussion of Characteristic Nondimensional Numbers* for details). As Ma ranges from 10^3 to 10^6 in our experiments, this scaling suggests that the no-slip limit, $u_I \ll U$, can be reached for very low surfactant concentrations, as shown by our simulations and suggested by our experiments. The scaling also suggests that an increase in g leads to an increase in u_I, as found in both simulations and experiments. In general $\Gamma(x)$ can have a nonlinear profile (41). As discussed in *SI Analysis and Discussion of*

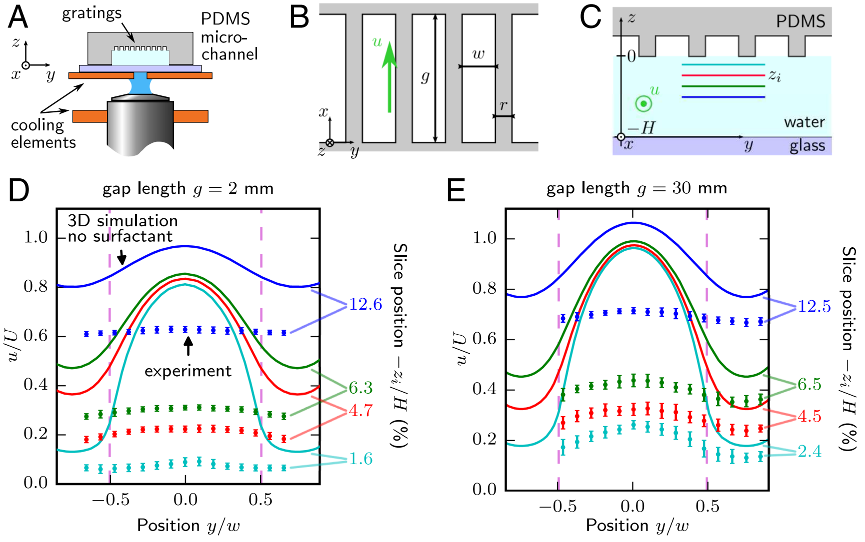

Fig. 3. μ-PIV setup and experimental velocity measurements with constant background flow and comparison with ideal 3D surfactant-free simulations. (*A*) Side view of the inverted PDMS microchannel with a textured SHS on top. The microchannel is in contact with cooling elements and lies above the water objective of the confocal microscope. (*B*) Geometry of the stream-wise parallel rectangular gratings forming the SHS. (*C*) Cross-section at $x = g/2$ of the microchannel. The measuring planes of the μ-PIV at heights z_i are indicated with different colors. (*D*) Lateral distribution of the stream-wise velocity at different heights z_i from the plastron, in the case of short lanes $g = 2$ mm. The profile is centered on a grating, with the edges of the ridges in dashed magenta lines. Experiments (symbols) show no signicant slip at the plastron, contrary to the strong slip predicted by 3D surfactant-free simulations (lines) for which the velocity is sampled at the same position z_i. (*E*) Same as in *D* in the case of long lanes $g = 30$ mm. Slip velocity at the plastron is still 85% smaller than predictions from surfactant-free simulations. For *D* and *E*, positions along z of the experimental imaging planes and sampling planes in simulations are given in percentage of the total chamber height, with $H = 130$ µm and 100 µm for the chambers in *D* and *E*, respectively. Positions along y are normalized by the gap width $w = 40$ µm for both *D* and *E*.

Characteristic Nondimensional Numbers, this does not affect the key findings of this study.

Pressure-Relaxation Experiments for Surfactant Effect

To prove experimentally the surfactant hypothesis while circumventing the difficulty of removing traces of surfactants, we designed time-dependent pressure-relaxation experiments to reveal in situ the presence of surfactant-induced stresses. All of the experiments were conducted with the apparatus shown in Fig. 3 *A–C*, with controlled temperature and interface deflection. These experiments began with a "loading phase," during which the flow was driven by a fixed, strong pressure gradient and allowed to reach steady state (*SI Experimental Protocols* and Tables S6 and S7). The driving pressure was then rapidly decreased to zero while keeping the hydrostatic pressure approximately constant. The change in background pressure gradient was simply achieved by moving the stage onto which the inlet reservoir was attached to the exact level for which both inlet and outlet water levels were at the same vertical position. The motion of the stage was conducted rapidly, within less than 4 s. During the loading phase, which was maintained for 4 min to ensure a steady state was reached, we measured a Poiseuille profile in the microchannel (Fig. S2), giving a mean load speed U (see *SI Experimental Protocols* for details on the technique used to measure U). Our measurements do not reveal significant slip on the SHS side during the loading phase. However, a clear backflow, with negative values (shown in blue in Fig. 4*A*), can be observed after the background pressure gradient vanishes (Movie S1).

Fig. 4*A* shows the time evolution of the lateral profile of the stream-wise velocity measured at $x = g/2$ and $z = -5\,\mu\mathrm{m}$ for a grating with $g = 30\,\mathrm{mm}$. The background pressure gradient decreases from a large constant value during the loading phase (mean load speed in the microchannel $U \approx 4.1\,\mathrm{mm{\cdot}s^{-1}}$ for $t \le 5\,\mathrm{s}$) to zero at $t = 7.2\,\mathrm{s}$. As the flow is in the Stokes regime ($Re = HU/\nu < 1$, with ν the kinematic viscosity), we expect that, in the absence of surfactants, the velocity should decrease from positive values to zero instantaneously and everywhere as soon as the forcing vanishes. This monotonic behavior can be observed in Fig. 4*A* for the velocity measured above the ridge (green triangles in Fig. 4*B*) and also above wetted gratings (Movie S2). In contrast, the velocity above the plastron (plotted in red and blue in Fig. 4*B* for the middle of the left and right gratings, respectively) decreases sharply to large negative values during the stage motion, corresponding to a flow opposed to the background pressure gradient. This backflow persists for a long time after the background pressure gradient vanishes. In this experiment, it decays over ≈1 min. The same qualitative results and trends are obtained independently of the choice of grating and the direction and intensity of the loading flow, as long as it is sufficiently strong.

During the loading phase, owing to large advection in the flow compared with diffusion and adsorption/desorption kinetics, surfactants at the interface are transported toward the downstream stagnation point of the lane. The concentration of surfactants increases significantly near this point, whereas it decreases everywhere else along the interface. This regime is likely to be analogous to the "stagnant cap regime" described for air bubbles rising in water (41). When the background pressure gradient vanishes, the surfactant-induced stresses are not opposed by viscous stresses any longer, and a Marangoni backflow develops to homogenize the surfactant concentration at the plastron, as shown in Fig. 4*B*. A shear flow establishes across the chamber height, owing to the wall shear stress on the opposite side of the plastron ($z = -H$). As the distribution of surfactant becomes more uniform, surfactant-induced stresses decrease and the backflow diminishes, as shown by the nonlinear temporal trend in Fig. 4*B*.

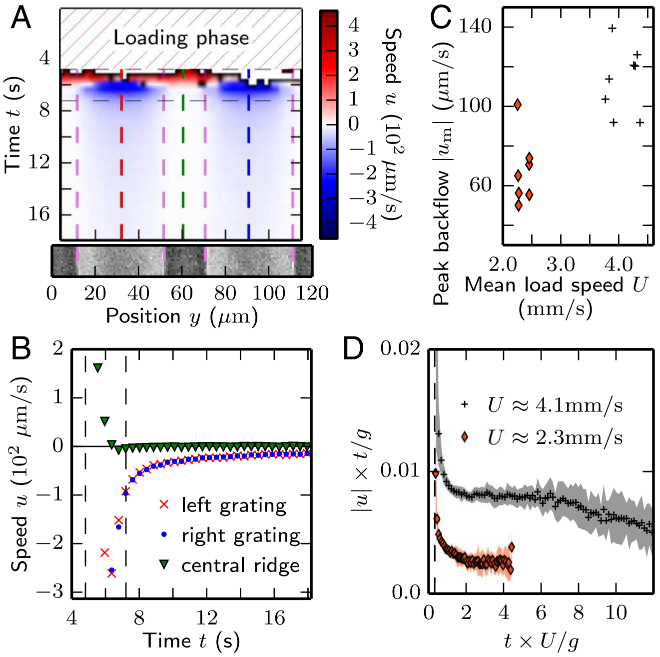

Fig. 4. Velocity measurements in pressure-relaxation experiments. (*A*) Kymograph showing the time evolution of the lateral profile of the midgap stream-wise velocity measured at ($x = g/2$, $z = -5\,\mu\mathrm{m}$) after a constant loading speed $U \approx 4.1\,\mathrm{mm{\cdot}s^{-1}}$. The two horizontal black dashed lines indicate the start and end of the pressure-head reduction to zero. *A*, *Bottom Inset* shows the position of the two gratings studied (appearing in light gray). The kymograph clearly shows a strong backflow over the lanes but not over the ridge (Movie S1). (*B*) Profiles from *A* taken along the red, blue, and green dashed vertical lines at the centerline of each grating and of the ridge, respectively. Red symbols are hidden by blue symbols as both gratings have the same profile. The SDs of all of the data are smaller than the symbol size. (*C*) Peak backflow velocity measured when the background pressure vanishes (corresponding to the second vertical dashed line in *B*), vs. the mean load speed for the two sets of experiments conducted for $U \approx 2.3\,\mathrm{mm{\cdot}s^{-1}}$ and $U \approx 4.1\,\mathrm{mm{\cdot}s^{-1}}$ (symbols as in D). (*D*) Ensemble average of the normalized backflow velocity multiplied by nondimensional time for the two sets of experiments, as a function of the nondimensional time. Standard deviations are shown in lighter shading.

We find that the maximum velocity of the backflow $|u_\mathrm{m}|$, measured when the background pressure gradient vanishes ($t \approx 7\,\mathrm{s}$), increases with the magnitude of the mean load speed U, as shown in Fig. 4*C*. This is consistent with a sharpening of the concentration gradient near the downstream stagnation point at higher background pressure gradients during the loading phase, which then results in stronger Marangoni stresses driving the backflow. The observation that the plastron always displays a transient that reverses direction relating to the loading flow is a strong indication that Marangoni stresses are driven by surfactant accumulation, rather than by thermal gradients set up by laser or by other elements of the experimental apparatus (discussion in *SI Experimental Protocols*).

To provide additional support to the surfactant hypothesis, as well as to show that the occurrence of the backflow is largely independent of the type of surfactant (and therefore of the associated kinetics), we developed a model for the backflow and compare the resulting scaling for the plastron velocity to experimental results. As surfactant diffusion is initially negligible at the air–water interface compared with advection, we model the backflow using a one-dimensional time-dependent advection equation for the interfacial surfactant concentration (*SI Model for Pressure-Relaxation Experiments*). We assume adsorption/desorption fluxes are also negligible. These hypotheses correspond to the stagnant cap regime (41). The surfactant transport equation is coupled with a viscous–Marangoni stress balance. Using a similarity solution, we find that the magnitude of the backflow decreases in time such that $|u| \propto 1/t$, which is in agreement with the experimental results plotted in Fig. 4*D* in nondimensional form. Fig. 4*D* shows the time evolution of the ensemble average (symbols) and SDs (light shadings) of the normalized backflow velocity $|u|/U$ multiplied by $t/(g/U)$. We show data for two sets of experiments conducted with $U \approx 2.3\,\mathrm{mm{\cdot}s^{-1}}$ and $U \approx 4.1\,\mathrm{mm{\cdot}s^{-1}}$ in the loading phase, plotted respectively in orange and black. The model is not valid at early time, $tU/g \leq 1$, due to the noninstantaneous decrease of the background pressure gradient occurring between the two vertical dashed lines, owing to the finite time required for the stage motion (≈3–4 s). At late times $tU/g \geq 6$, the plateau observed for the large forcing experiments seems to end, as the data decrease again. This is consistent with the fact that the model, which assumes a semi-infinite lane, is not valid at late times when the effect of the opposite stagnation point is felt. Moreover, we note in Fig. 4*D* that the value of the plateau region increases with U. This result contrasts with the model that predicts the backflow velocity depends only on the local concentration gradient. This indicates nonlinearities not taken into account by the model, such as strong variations in the initial surfactant distribution for different U or that the interface is not completely in the stagnant cap regime (discussion in *SI Model for Pressure-Relaxation Experiments*).

Outlook

An important conclusion is that quantitative models of superhydrophobic slip must also account for surfactant effects, or they can drastically overestimate drag reduction. This is consistent, for example, with established approaches for predicting the rise speed of small gas bubbles, which are known to be sensitive to surfactant-induced Marangoni stresses (41).

From a practical standpoint, our numerical and experimental findings point to the need to focus efforts on textures that have large distances between upstream and downstream stagnation points and that minimize locations where surfactant can accumulate. This explains why several experiments have reported that the greatest drag reduction was achieved with either long gratings (16, 42) or microposts or random textures having large gas fraction (up to 99%) (8, 12). Some of the largest slip lengths were achieved with annular gratings in a circular rheometer (12). Annular gratings are effectively infinitely long lanes, without stagnation points, thus preventing the formation of surfactant concentration gradient and adverse Marangoni stresses. However, applications of SHSs with annular geometries are limited. Textures with low gas fraction and small stream-wise interface length g (which can resist larger fluid pressure and can be easier to manufacture) have reported slip several times smaller than expected from surfactant-free theory (e.g., the meshes and posts in refs. 25 and 38 have gas fractions 26–55%; the gratings in ref. 24 have $g \simeq 1$ mm). In turbulent flows (such as in ref. 16) mixing is expected to enhance surfactant fluxes, potentially inducing a qualitative change in Marangoni stress. To enable general predictions, it would be important to extend existing effective slip models (27, 29, 34) to include surfactant.

From a methodological standpoint, our experimental tests involving pressure relaxation also provide a simple way of measuring the magnitude of surfactant-induced effects, for an SHS immersed in a given liquid. The presence of a backflow immediately reveals a plastron whose dynamics are strongly susceptible to surfactants. This can be a useful test to guide the design of SHSs that are unimpaired by surfactant Marangoni stresses. Overall, we believe this work constitutes a significant advance in our fundamental understanding of superhydrophobic drag reduction, moving the field closer to SHSs that perform reliably in realistic applications.

Materials and Methods

Numerical Simulations. The simulations solve six partial differential equations for the transport of mass, momentum, and surfactant in the fluid interior and along the air–water interface (41) (see *SI Model* for details). The ridges and bottom walls have a no-slip boundary condition. At the air–water interface we enforce continuity of the viscous stress with the Marangoni stress and continuity of the bulk velocity with the interfacial velocity. Air drag is negligible here and is not considered. Surfactants present in the interior layer near the plastron are adsorbed or desorbed following specific kinetics. We have chosen a well-characterized surfactant, namely SDS as our case study surfactant. The SDS properties are well described by Frumkin kinetics (39). These equations are solved using a finite-element method from COMSOL Multiphysics, with a Poiseuille profile as inlet condition and a weak constraint added to a free-slip boundary condition to capture the Marangoni effects at the air–water interface. A refined mesh at the interface and near the endpoints, together with higher-order elements, guarantees numerical accuracy (*SI Materials and Methods*).

Microchannel Preparation. Microchannels of PDMS (Sylgard 184) with a top surface consisting of long rectangular gratings were fabricated from a master mold obtained by photolithography (43) (*SI Experimental Protocols*). They were bonded to glass coverslips through untreated PDMS adhesion. All glass slides and tubing were washed thoroughly with purified water. The cleaning protocol is described in *SI Experimental Protocols*.

Laser Scanning Confocal Microscopy. To measure the fluid velocity, we washed and suspended microbeads (LifeTechnologies FluoSphere carboxylate 0.5-μm diameter yellow/green 505/515) in purified water (using the Milli Q water purification system; EMD Millipore) and injected the resulting solution at 0.08% solids in the chamber. Using a spinning-disk confocal microscope for green fluorescence (Yokogawa CSU-X1 mounted on a Zeiss Axio Observer Z1, with laser line 488 nm with power at the objective level less than 155 μW), we captured image sequences at distinct z planes of the chamber on a high-sensitivity EMCCD (Photometrics Evolve 512 Delta), at a rate of ≈10 frames per second. We used a water objective (Olympus LUMPLFLN 60XW) to guarantee a proper determination of the position of the imaging plane and allow deep imaging without loss of fluorescence brightness. A bright-field picture of the ridges and gratings allowed us to determine the position of the SHS with respect to the field of imaging. To prevent heating of the microchannel during imaging, it was placed in thermal contact with a heat-conducting plate, itself in contact with Peltier elements driven by a thermoelectric controller (Laird Technologies MTTC1410). To absorb the heat from the objective, we mounted a second Peltier element around it, coupled to a similar controller to maintain its temperature at 23± 0.1 °C. Fans were also used to cool the hot plates of the Peltier elements.

Flow Control. To ensure the driving pressure had no fluctuations, the flow of water with fluorescent particles was driven by gravity. The microchannel was connected with flexible tubing (Tygon ND-100-80) to two reservoirs (polypropylene tube; Eppendorf), whose absolute and relative heights could be varied independently. By varying the absolute position of the two reservoirs while keeping their relative position such that no flow was observable in the chamber, we minimized the curvature of the air–water interface in the chamber by adjusting the hydrostatic pressure. The maximum interface deflection over the width of the interface was less than 2 μm. By adjusting the relative position of the reservoirs, varying background pressure gradients could be imposed in the channel to generate flow. The variation of relative position was performed using a motorized stage (Thorlabs NRT150/M) driven by a precision controller (Thorlabs APT BSC201), guaranteeing a position precision of 2 μm and rapid changes in pressure gradients (maximum acceleration, 50 $\mathrm{mm{\cdot}s^{-2}}$; maximum speed, 50 $\mathrm{mm{\cdot}s^{-1}}$).

Image Analysis and μ-PIV. The images were analyzed with MATLAB, using a customized version of the PIV toolbox, mPIV (44). The correlation functions between adjacent frames were rescaled to correct for nonuniform time steps between frames, and the resulting correlation functions were added over a pack of 10–30 frames before searching for peak correlations. This allowed us to correct for Brownian motion uncertainties. For the time-relaxation experiments, the velocity profile in the chamber during the loading phase at high flow rate was obtained by measuring the mean length of the fluorescent particle streaks on the image and dividing by the exposure time.

ACKNOWLEDGMENTS. We thank D. Page-Croft and the engineers of the G. K. Batchelor Laboratory for their technical support. We gratefully acknowledge financial support from the Raymond and Beverly Sackler Foundation (R.E.G. and F.J.P.); the Engineering and Physical Sciences Research Council Grant 1196197 (to R.E.G. and F.J.P.); the European Research Council Grant 247333 (to R.E.G.); Mines ParisTech (F.J.P.); the Schlumberger Chair Fund (R.E.G.); and the University of California, Santa Barbara, Senate and California NanoSystems Institute Challenge Grant (to P.L.-F.); as well as from Churchill College (P.L.-F.) and Magdalene College (J.R.L.), Cambridge, United Kingdom.

1. Quéré D (2008) Wetting and roughness. *Ann Rev Mater Res* 38:71–99.
2. Rothstein JP (2010) Slip on superhydrophobic surfaces. *Ann Rev Fluid Mech* 42:89–109.
3. Samaha MA, Tafreshi HV, Gad-el Hak M (2012) Superhydrophobic surfaces: From the lotus leaf to the submarine. *C R Mécanique* 340:18–34.
4. Liu TL, Kim CJ (2014) Turning a surface superrepellent even to completely wetting liquids. *Science* 346:1096–1100.
5. Tian X, Verho T, Ras RHA (2016) Moving superhydrophobic surfaces toward real-world applications. *Science* 352:142–143.
6. Ou J, Perot B, Rothstein JP (2004) Laminar drag reduction in microchannels using ultrahydrophobic surfaces. *Phys Fluids* 16:4635–4643.
7. Ou J, Rothstein JP (2005) Direct velocity measurements of the flow past drag-reducing ultrahydrophobic surfaces. *Phys Fluids* 17:103606.
8. Choi CH, Kim CJ (2006) Large slip of aqueous liquid flow over a nanoengineered superhydrophobic surface. *Phys Rev Lett* 96:066001.
9. Joseph P, et al. (2006) Slippage of water past superhydrophobic carbon nanotube forests in microchannels. *Phys Rev Lett* 97:156104.
10. Tsai P, et al. (2009) Quantifying effective slip length over micropatterned hydrophobic surfaces. *Phys Fluids* 21:112002.
11. Karatay E, et al. (2013) Control of slippage with tunable bubble mattresses. *Proc Natl Acad Sci USA* 110:8422–8426.
12. Lee C, Choi CH, Kim CJ (2008) Structured surfaces for a giant liquid slip. *Phys Rev Lett* 101:064501.
13. Daniello RJ, Waterhouse NE, Rothstein JP (2009) Drag reduction in turbulent flows over superhydrophobic surfaces. *Phys Fluids* 21:085103.
14. Woolford B, Prince J, Maynes D, Webb BW (2009) Particle image velocimetry characterization of turbulent channel flow with rib patterned superhydrophobic walls. *Phys Fluids* 21:085106.
15. Jung YC, Bhushan B (2010) Biomimetic structures for fluid drag reduction in laminar and turbulent flows. *J Phys Condens Matter* 22:035104.
16. Park H, Sun G, Kim CJ (2014) Superhydrophobic turbulent drag reduction as a function of surface grating parameters. *J Fluid Mech* 747:722–734.
17. Lee C, Choi CH, Kim CJ (2016) Superhydrophobic drag reduction in laminar flows: A critical review. *Exp Fluids* 57:176.
18. Watanabe K, Udagawa Y, Udagawa H (1999) Drag reduction of Newtonian fluid in a circular pipe with a highly water-repellent wall. *J Fluid Mech* 381:225–238.
19. Gogte S, et al. (2005) Effective slip on textured superhydrophobic surfaces. *Phys Fluids* 17:051701.
20. Henoch C, et al. (2006) Turbulent drag reduction using superhydrophobic surfaces. *3rd AIAA Flow Control Conference* (American Institute of Aeronautics and Astronautics, Inc., Reston, VA).
21. Zhao J, Du X, Shi X (2007) Experimental research on friction-reduction with superhydrophobic surfaces. *J Mar Sci Appl* 6:58–61.
22. Peguero C, Breuer K (2009) On drag reduction in turbulent channel flow over superhydrophobic surfaces. *Advances in Turbulence XII*, ed Eckhardt B (Springer, Berlin), pp 233–236.
23. Kim TJ, Hidrovo C (2012) Pressure and partial wetting effects on superhydrophobic friction reduction in microchannel flow. *Phys Fluids* 24:112003.
24. Bolognesi G, Cottin-Bizonne C, Pirat C (2014) Evidence of slippage breakdown for a superhydrophobic microchannel. *Phys Fluids* 26:082004.
25. Gruncell B (2014) PhD thesis (University of Southampton, Southampton, UK).
26. Philip JR (1972) Flows satisfying mixed no-slip and no-shear conditions. *Z Angew Math Physik* 23:353–372.
27. Philip JR (1972) Integral properties of flows satisfying mixed no-slip and no-shear conditions. *Z Angew Math Physik* 23:960–968.
28. Cottin-Bizonne C, Barentin C, Charlaix É, Bocquet L, Barrat JL (2004) Dynamics of simple liquids at heterogeneous surfaces: Molecular-dynamics simulations and hydrodynamic description. *Eur Phys J E* 15:427–438.
29. Lauga E, Stone HA (2003) Effective slip in pressure-driven Stokes flow. *J Fluid Mech* 489:55–77.
30. Ybert C, Barentin C, Cottin-Bizonne C, Joseph P, Bocquet L (2007) Achieving large slip with superhydrophobic surfaces: Scaling laws for generic geometries. *Phys Fluids* 19:123601.
31. Sbragaglia M, Prosperetti A (2007) A note on the effective slip properties for microchannel flows with ultrahydrophobic surfaces. *Phys Fluids* 19:043603.
32. Teo CJ, Khoo BC (2010) Flow past superhydrophobic surfaces containing longitudinal grooves: Effects of interface curvature. *Microfluid Nanofluid* 9:499–511.
33. Davis AMJ, Lauga E (2009) Geometric transition in friction for flow over a bubble mattress. *Phys Fluids* 21:011701.
34. Crowdy DG (2016) Analytical formulae for longitudinal slip lengths over unidirectional superhydrophobic surfaces with curved menisci. *J Fluid Mech* 791:R7.
35. Kropfli RA, et al. (1999) Relationships between strong internal waves in the coastal zone and their radar and radiometric signatures. *J Geophys Res* 104:3133–3148.
36. Lewis MA (1991) Chronic and sublethal toxicities of surfactants to aquatic animals: A review and risk assessment. *Water Res* 25:101–113.
37. Facchini MC, Decesari S, Mircea M, Fuzzi S, Loglio G (2000) Surface tension of atmospheric wet aerosol and cloud/fog droplets in relation to their organic carbon content and chemical composition. *Atmos Env* 34:4853–4857.
38. Schäffel D, Koynov K, Vollmer D, Butt HJ, Schönecker C (2016) Local flow field and slip length of superhydrophobic surfaces. *Phys Rev Lett* 116:134501.
39. Prosser AJ, Franses EI (2001) Adsorption and surface tension of ionic surfactants at the air–water interface: Review and evaluation of equilibrium models. *Colloids Surf A* 178:1–40.
40. Chang CH, Franses EI (1995) Adsorption dynamics of surfactants at the air/water interface: A critical review of mathematical models, data, and mechanisms. *Colloids Surf A* 100:1–45.
41. Palaparthi R, Papageorgiou DT, Maldarelli C (2006) Theory and experiments on the stagnant cap regime in the motion of spherical surfactant-laden bubbles. *J Fluid Mech* 559:1–44.
42. Truesdell R, Mammoli A, Vorobieff P, van Swol F, Brinker CJ (2006) Drag reduction on a patterned superhydrophobic surface. *Phys Rev Lett* 97:044504.
43. McDonald JC, Whitesides GM (2002) Poly(dimethylsiloxane) as a material for fabricating microfluidic devices. *Acc Chem Res* 35:491–499.
44. Mori N, Chang KA (2003) Introduction to mpiv. Available at www.oceanwave.jp/softwares/mpiv. Accessed May 15, 2015.
45. Rosen MJ, Kunjappu JT (2012) *Surfactants and Interfacial Phenomena* (Wiley, Hoboken, NJ).
46. Hourlier-Fargette A, Antkowiak A, Chateauminois A, Neukirch S (2017) Role of uncrosslinked chains in droplets dynamics on silicone elastomers. *Soft Matter* 13:3484–3491.